Journal of Materials Chemistry A

Enhanced Thermoelectric Performance of p-type Mg2Sn Single Crystals via Multi-scale Defect Engineering

Journal:	*Journal of Materials Chemistry A*
Manuscript ID	TA-ART-11-2022-008557.R1
Article Type:	Paper
Date Submitted by the Author:	16-Dec-2022
Complete List of Authors:	Huang, Zhicheng; Tohoku University, Applied Physics Hayashi, Kei; Tohoku University, Department of Applied Physics, Graduate School of Engineering Saito, Wataru; Tohoku University, Applied physics Pei, Jun; Tsinghua University, State Key Laboratory of New Ceramics and Fine Processing, School of Materials Science and Engineering Li, Jing-Feng; Tsinghua University, State Key Laboratory of New Ceramics and Fine Processing, School of Materials Science and Engineering Miyazaki, Yuzuru; Tohoku University, Department of Applied Physics, Graduate School of Engineering

ARTICLE

Enhanced Thermoelectric Performance of p-type Mg_2Sn Single Crystals via Multi-scale Defect Engineering†

Received 00th January 20xx,
Accepted 00th January 20xx

DOI: 10.1039/x0xx00000x

Zhicheng Huang,[a] Kei Hayashi,*[a] Wataru Saito,[a] Jun Pei,[b] Jing-Feng Li,[ab] and Yuzuru Miyazaki [a]

Mg_2Sn is a promising mid-temperature thermoelectric (TE) material consisting of earth-abundant, low-cost, and non-toxic elements. Currently, the TE performance of p-type Mg_2Sn is still poor due to a lower power factor (PF) and a higher lattice thermal conductivity (κ_{lat}) than those of n-type Mg_2Sn. To overcome these disadvantages, we synthesized Li-doped Mg_2Sn single crystals (SCs) by the melting method. The Li-doping successfully changed the conduction of the Mg_2Sn SC from an n-type to a p-type. The Li-doped Mg_2Sn SCs contained Mg vacancy, dislocation cores, and Sn-rich precipitates. These multi-scale defects in the Li-doped Mg_2Sn SCs did not deteriorate carrier mobility, whereas they effectively scattered phonons with a wide range of frequencies. Since grain boundaries did not exist in the Li-doped Mg_2Sn SC, a higher carrier mobility and a higher PF were achieved compared with other p-type Mg_2Sn polycrystals (PCs) and SCs. Moreover, the κ_{lat} of the Li-doped Mg_2Sn SC was lower than that of the p-type Mg_2Sn PCs and SCs. Owing to the enhanced PF and the reduced κ_{lat}, a maximum dimensionless figure-of-merit zT of ~0.38 at 700 K was achieved for the p-type Li-doped Mg_2Sn SC with a Li content of 2.5%, the highest value for a p-type Mg_2Sn ever reported.

Introduction

Thermoelectric (TE) materials have attracted increasing attention because they can directly convert waste heat to electricity via the Seebeck effect.[1–4] The performance of a TE material is generally gauged by the dimensionless figure-of-merit zT (= $S^2\sigma T/\kappa_{tot}$) and power factor PF (= $S^2\sigma$), where S, σ, T, and κ_{tot} denote the Seebeck coefficient, electrical conductivity, absolute temperature, and total thermal conductivity, respectively. κ_{tot} is the sum of the electronic thermal conductivity (κ_{el}), bipolar thermal conductivity (κ_{bip}), and lattice thermal conductivity (κ_{lat}). Two aspects should be considered to facilitate the application of TE materials: achieving high zT and PF values to increase energy conversion efficiency by optimizing the interrelationships among the TE properties, and exploring cost-effective TE materials using earth-abundant, low-cost, and non-toxic elements.

Among the considered materials, Mg_2Sn and its derivatives $Mg_2(Si,Ge,Sn)$ are potential TE materials for operation at moderate temperatures between 400 K and 800 K.[5–34] Good TE performances (zT ~ 0.9 at 750 K) have been reported for n-type Mg_2Sn utilizing point defects and carrier optimization.[26,27] Among the n-type Mg_2Sn samples, undoped, B-doped, and Sb-doped Mg_2Sn single crystals (SCs),[22–24,34] Bi-doped Mg_2Sn polycrystals (PCs),[26] and Sb-doped Mg_2Sn PCs[27] prepared by applying physical and chemical pressure were found to contain Mg vacancy (V_{Mg}) as a point defect. The V_{Mg} acted as a scattering center of phonons, decreasing κ_{lat}. For example, the B-doping introduced V_{Mg} at the fraction of 13.4(47)% and dislocation cores into the Mg_2Sn SC, reducing κ_{lat} to a predicted minimum value (κ_{min} ~ 0.65 W m^{-1} K^{-1} [13]) at 650 K.[24] Furthermore, the Bi-doping or Sb-doping increased the electron carrier concentration up to an optimal value, enhancing PF.[23,26,27,34] In particular, the Sb-doped Mg_2Sn SC exhibited the highest PF due to a high Hall carrier mobility (μ_H),[23,24] according to a general trend that the absence of grain boundary scattering in an SC leads to a higher μ_H compared to a PC with the same composition.[35,36]

On the contrary, p-type Mg_2Sn has inferior TE properties for practical applications. Various elements such as Ag,[5] Li,[19,20] Ga,[25] Cu,[29] and Na[30] were used to introduce the hole carriers into Mg_2Sn. Many efforts have been devoted to enhancing the TE performance of p-type Mg_2Sn. Chen et al.[5] prepared p-type Ag-doped Mg_2Sn large-grain PCs with finely dispersed eutectic MgAg phase; its maximum zT value reached ~0.3 at 500 K due to the reduction of κ_{lat}. Hasbuna et al.[19] prepared p-type Li-doped Mg_2Sn PCs by ball milling with a maximum zT value of ~0.3 at 700 K by enhancing σ and PF, indicating that Li is an effective p-type dopant. More recently, we prepared p-type Ga-doped Mg_2Sn SCs by melting method.[25] Different from the above p-type Mg_2Sn PCs, the Ga-doped Mg_2Sn SCs contained V_{Mg} at the fraction of 7.0(19)-13.4(26)%. Consequently, an $Mg_2Sn_{0.98}Ga_{0.02}$ SC displayed lower κ_{tot} than the Ag-doped and Li-doped Mg_2Sn PCs. Similar to the Sb-doped Mg_2Sn SC,[23] the $Mg_2Sn_{0.98}Ga_{0.02}$ SC had a higher μ_H than the Li-doped Mg_2Sn PC; however, its PF was lower due to its lower hole carrier concentration n (Table

[a] Department of Applied Physics, Graduate School of Engineering, Tohoku University, Sendai 980-8579, Japan. E-mail address: kei.hayashi.b5@tohoku.ac.jp (K. Hayashi)
[b] State Key Laboratory of New Ceramics and Fine Processing, School of Materials Science and Engineering, Tsinghua University, Beijing, 100084, China.
† Electronic Supplementary Information (ESI) available: Laue XRD; SC-XRD; TEM observation; Electronic Thermal Conductivity; Bipolar Thermal Conductivity; and Lattice Thermal Conductivity. See DOI: 10.1039/x0xx00000x

1). Thus, the $Mg_2Sn_{0.98}Ga_{0.02}$ SC showed a lower zT (~0.18 at 450 K) than the Li-doped Mg_2Sn PC.

To further improve the TE performance of p-type Mg_2Sn SCs, we adopted two strategies; (1) Li element was selected as an effective p-type dopant for Mg_2Sn SCs to enhance PF; and (2) multi-scale defects in addition to V_{Mg} were introduced into the Mg_2Sn SCs to reduce κ_{lat} because the lowest κ_{lat} of the $Mg_2Sn_{0.98}Ga_{0.02}$ SC with V_{Mg} (1.8 W m^{-1} K^{-1} at 650 K [25]) was still higher than the κ_{min}. In this study, a series of p-type Li-doped Mg_2Sn SCs were synthesized by the melting method, a convenient and inexpensive method to prepare SCs.[22–25,37,38] Interestingly, the Li-doped Mg_2Sn SCs contained V_{Mg} as well as dislocation cores (DCs) and nanoscale Sn-rich precipitates as lattice defects. We found that the Li-doping to Mg_2Sn SCs exhibited a high μ_H and a low κ_{lat}. The mechanisms for attaining high μ_H and low κ_{lat} are discussed from the viewpoint of carrier and phonon scattering. Through synergistically optimizing electronic and thermal transport properties, we achieved a maximum zT of ~0.38 at 700 K for the Li-doped Mg_2Sn SC with the Li content of 2.5%, which is the record value among the p-type Mg_2Sn SCs and PCs.

Experimental

Sample preparation

Mg grains (4N, Mitsuwa Chemicals Co. Ltd., ~Φ4 × 4t mm), Sn powder (4N, Kojundo Chemical Lab., 63 μm pass), and Li rod (3N, Sigma-Aldrich Co. Ltd., ~Φ12.7 mm) were weighted according to the nominal composition of $Mg_{2-x}Li_xSn$ (x = 0.005, 0.015, 0.020, and 0.025). The weighed materials were individually loaded into a BN-coated alumina crucible in a glove box under an argon atmosphere with an oxygen level below 0.1 ppm. The alumina crucible was enclosed in a quartz tube evacuated to a pressure of ~10^{-6} Pa and then filled with an Ar atmosphere of 0.16 MPa to apply the physical pressure. By setting the quartz tube in an electric furnace with a vertical temperature gradient, each material was melted at 1123 K, cooled at a rate of 2 K/h to 1023 K, and then cooled to room temperature (RT) over 9 h. The typical size of the obtained $Mg_{2-x}Li_xSn$ ingots was ~Φ10 mm×L20 mm, and their lower part ranging from 2 to 7 mm from the bottom was used for the evaluation (Figure S1a).

Sample characterization

The crystalline phase and crystallinity of the $Mg_{2-x}Li_xSn$ ingots were investigated by powder X-ray diffraction (XRD; D8 ADVANCE, Bruker AXS) and Laue XRD (RINT-IP/S, Rigaku). Due to the problematic crystal structure refinement using the powder XRD patterns of the $Mg_{2-x}Li_xSn$ ingots, as in the case of Mg_2Si,[39,40] the lattice parameters and the V_{Mg} fraction were evaluated by single-crystal XRD (SC-XRD; D8 QUEST, Bruker AXS), using a small $Mg_{2-x}Li_xSn$ SC (typically, 30×60×70 μm^3) taken from each ingot (see the Supporting Information for details of the structural analysis). Single-crystal structure refinement was performed using the JANA2006 crystallographic computing code.[41] The microstructure was observed using a scanning electron microscope equipped with an energy-dispersive X-ray spectrometer (SEM-EDX; JSM-IT100, JEOL). In addition, transmission electron microscopy (TEM), scanning TEM (STEM), atomic-resolution high-angle annular dark-field STEM (HAADF-STEM) observations, and energy dispersive X-ray spectroscopy (EDS) were conducted using an atomic-resolution analytical electron microscope (JEM-ARM200F, JEOL). The XRD measurements and TEM-EDS observations were all performed at RT.

The S and σ values of the $Mg_{2-x}Li_xSn$ ingots were measured from 300 K to 700 K under a vacuum using an automated thermoelectric tester (RZ2001i, Ozawa Science Co. Ltd.). The Hall coefficient R_H was measured at RT by sweeping a magnetic field from −5.0 T to 5.0 T using a physical properties measurement system (PPMS, Quantum Design). The carrier concentration n was obtained by $n = |1/(eR_H)|$, and the Hall carrier mobility μ_H was calculated by $\mu_H = \sigma R_H$, where e is the electric charge. The typical sample size used for the S and σ measurements was 2.5×2.5×8 mm^3, and that for the Hall measurements was 2.5×6×0.8 mm^3. The total thermal conductivity κ_{tot} was calculated using the relation $\kappa_{tot} = \rho_s D C_p$, where ρ_s, D, and C_p are the sample density, thermal diffusivity, and specific heat capacity, respectively. The density was determined by $\rho_s = m/V$, where m is the mass and V is the volume. The D and C_p of the samples were measured from 300 K to 700 K under a vacuum using a laser flash apparatus (TC-7000, ULVAC-RIKO). The sample size for the D and C_p measurements was typically ~Φ10 mm×L2 mm.

Electronic band calculation

We used the Korringa–Kohn–Rostoker (KKR) method with the coherent potential approximation implemented in the AkaiKKR package[42] to calculate the electronic band structure of undoped Mg_2Sn and 2% Li-doped Mg_2Sn without any vacancy defects. The Perdew-Burke-Ernzerhof exchange-correlation potential was used for this calculation. The imaginary part at the Fermi level (E_F) was set to 10^{-4} Ry. The angular momentum cut-off was set at 2, i.e., s-, p-, and d-orbitals were considered. The lattice parameter was evaluated by optimizing a unit cell volume to have minimum total energy.

Results and discussion

Crystal structure

The crystallinity of the prepared $Mg_{2-x}Li_xSn$ (x = 0[25], 0.005, 0.015, 0.020, and 0.025) ingots was examined with the Laue XRD measurements (Figure S2a-e). The clear Laue XRD spots were observed as a simulation using a crystal structure with the $Fm\bar{3}m$ space group (Figure S2f), demonstrating that the $Mg_{2-x}Li_xSn$ ingots were all SCs.

The powder XRD patterns of the $Mg_{2-x}Li_xSn$ (x = 0[25], 0.005, 0.015, 0.020, and 0.025) SCs are depicted in Figure 1a. All the main XRD peaks were well-indexed to a cubic Mg_2Sn phase (PDF #07-0274; space group: $Fm\bar{3}m$). A trace of an Sn phase (PDF# 04-0673; marked with *) was observed in the enlarged XRD patterns at 35-40° for all SCs. SEM observations revealed

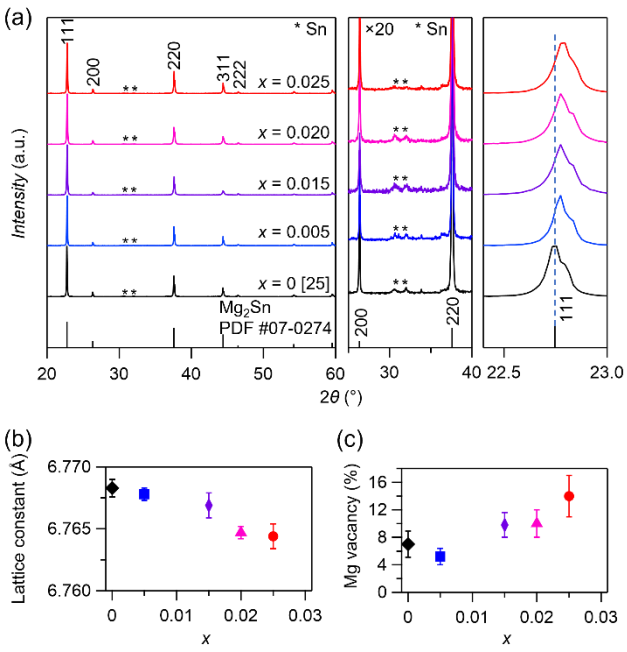

Figure 1. (a) Powder X-ray diffraction (XRD) patterns, along with the enlarged peaks at 25° ~ 40° and 22.5° ~ 23.0° . (b) Lattice constant and (c) the fraction of Mg vacancy (V_{Mg}) of the $Mg_{2-x}Li_xSn$ (x = 0[25], 0.005, 0.015, 0.020, and 0.025) SCs.

than the Sn secondary phase existed only at the edge area of each ingot (Figures S1b, b1, c, c1, and c2). To avoid an effect of the Sn secondary phase, the samples used for the physical-properties measurements were obtained from the center of each ingot (Figure S1a). As shown in the enlarged XRD patterns at 22.5-23.0° (Figure 1a(right)), the 111 peak of the Mg_2Sn phase slightly shifted to a higher angle after introducing Li, meaning that the Li-doping made the lattice constant smaller according to Bragg's law. It is reasonable because the atomic radius of Li (152 pm[43]) is smaller than that of Mg (160 pm[43]).

The lattice constant was determined by the SC-XRD measurements; it decreased from 6.7683(7) Å at x = 0 [25] to 6.7644(10) Å at x = 0.025 (Figure 1b). Moreover, the presence of V_{Mg} in the $Mg_{2-x}Li_xSn$ SCs was confirmed. The V_{Mg} fraction increased with increasing x; 7.0(19)% [25], 5.2(12)%, 9.8(18)%, 10(2)%, and 14(3)% for x = 0, 0.005, 0.015, 0.020, and 0.025 SCs, respectively (Figure 1c). (Other refined structural parameters are summarized in Table S1.) The inverse correlation between the lattice constant and V_{Mg} fraction can be explained by the effect of chemical pressure on the formation energy of V_{Mg}, as reported for the Sb-doped, B-doped, and Ga-doped Mg_2Sn SCs.[23-25,34]

Nanostructure

To investigate the nanostructure of the $Mg_{2-x}Li_xSn$ SCs, TEM and STEM observations for the x = 0.020 SC were performed. As shown in Figure 2a, light gray, dark gray, and black regions were identified in a low-magnification TEM image. The dark gray and black regions were embedded in the light gray region, and their sizes were <10 nm and 10-50 nm in diameter, respectively. Figure 2b is the medium-magnification TEM image of the R1 region in Figure 2a. In the image, light gray and dark gray regions are indicated by white dashed squares as an example (R2 and R3 regions, respectively). Such light gray and dark gray regions are attributed to a single-crystal region and a V_{Mg} region, respectively, for the undoped, Sb-doped, B-doped, and Ga-doped Mg_2Sn SCs, which contain V_{Mg} as a point defect.[22-25,34] It is reported that V_{Mg} does not exist in the single-crystal region, whereas V_{Mg} aggregates to form the dark gray regions symbolized by a striped pattern, namely, a Moiré pattern.[44,45] To examine the light gray and dark gray regions in the x = 0.020 SC,

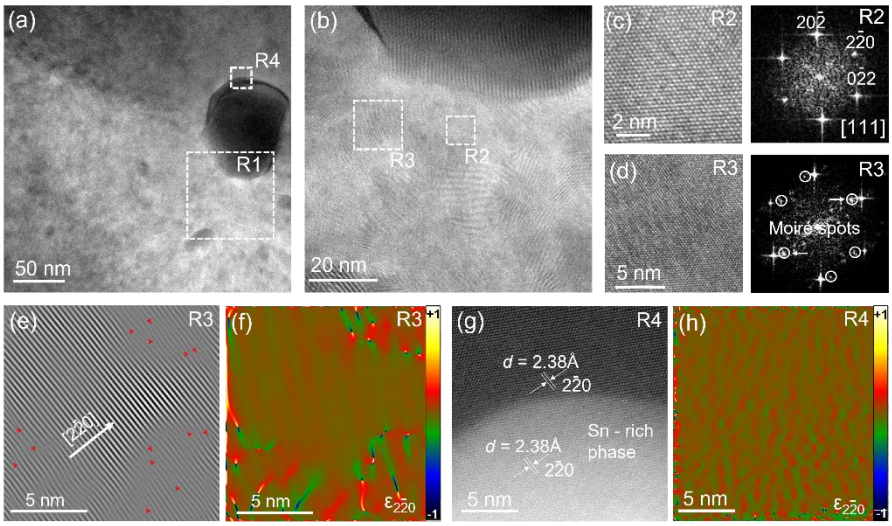

Figure 2. (a) Low-magnification transmission electron microscope (TEM) image of the $Mg_{1.980}Li_{0.020}Sn$ (x = 0.020) SC. (b) Mid-magnification TEM image of the R1 region in Figure 2a. (c) [Left] high-magnification TEM image and [Right] a fast Fourier transform (FFT) pattern of the single-crystal region (marked as the R2 region in Figure 2b). (d) [Left] high-magnification TEM image and [Right] an FFT pattern of the V_{Mg} region (marked as the R3 region in Figure 2b). (e) Filtered inverse FFT image of the R3 region using the two extra spots of the FFT pattern in Figure 2d [Right]. (f) Geometric phase analysis (GPA) image of the R3 region in Figure 2b. (g) High-angle annular dark-field scanning TEM image and (h) a GPA image of the R4 region in Figure 2a.

the R2 region in Figure 2b is magnified in Figure 2c (left), showing the regular arrangement of the Mg and Sn atoms in the (111) plane of the Mg_2Sn phase. Its fast Fourier transform (FFT) pattern confirmed a series of spots of the Mg_2Sn phase along the [111] direction (Figure 2c (right)). Figure 2d (left) shows the magnified image of the R3 region in Figure 2b; the dark gray region was the Moiré pattern. Therefore, we concluded that the light gray and dark gray regions were the single-crystal region and the V_{Mg} region, respectively.

An FFT pattern of the R3 region is shown in Figure 2d (right). There were extra spots (inside the white circles) near the spots of the Mg_2Sn phase. A filtered inverse FFT image was reproduced using one set of the extra spots (indicated by arrows) (Figure 2e). DCs were located around the V_{Mg} region, indicating that the interface between the single-crystal region and the V_{Mg} region was semi-coherent, similar to the undoped, Sb-doped, B-doped, and Ga-doped Mg_2Sn SCs.[22-25,34] The density of DCs was estimated to be 3.3×10^{16} m^{-2}. To further investigate strain variation around the V_{Mg} region, we performed geometric phase analysis (GPA), a semi-quantitative lattice image-processing approach to reveal spatially distributed strain fields.[46,47] Figure 2f shows the GPA result of the TEM image in Figure 2d (left). The high-strain centers (in yellow) were depicted in the vicinity of the DCs, indicating that the strain fields were induced by V_{Mg} and existed around the V_{Mg} region.

The black regions in low-magnification TEM images were also investigated. The size of the black regions was 10-50 nm in diameter (Figure 2a), confirmed in another low-magnification TEM image (Figure S3a). Figure 2g shows a HAADF-STEM image of the R4 region in Figure 2a. The contrast gradually changed from the bottom (corresponding to the black region) to the top (corresponding to the light gray region, i.e., the single-crystal region). Considering the *Z*-contrast nature of the HAADF-STEM imaging,[46,48] the black region can be attributed to a precipitate rich in heavier elements compared with the single-crystal region. The EDS analysis revealed a ratio of Mg:Sn of 1:2 at the black region, suggesting that the $Mg_{2-x}Li_xSn$ SCs contained the Sn-rich precipitate. Figure S3b shows an electron diffraction pattern of a selected area inside the white dash circle in Figure S3a. Although the selected area contained several black regions, only the spots with 3-fold symmetry were observed, similarly to the Mg_2Sn phase along the [111] direction. In other words, the Sn-rich precipitate had the same crystal structure as the Mg_2Sn phase. The interplanar spacing was determined to be 2.38 Å for both the Sn-rich precipitate and the single-crystal region (Figure 2g); this value agreed with the interplanar spacing between the (220) planes of the Mg_2Sn phase (2.41 Å; PDF #07-0274). From the above observations, the Sn-rich precipitate is an endotaxial nanostructure embedded in the single-crystal region; this was observed for the first time among the undoped and elementary-doped Mg_2Sn SCs prepared by the melting method.[22–25,34] The emergence of the Sn-rich precipitates by the Li-doping may be explained by the decrease of formation energy of an antisite defect that an Sn atom substitutes for the Mg site, Sn_{Mg}. In the present case, the prepared $Mg_{2-x}Li_xSn$ SCs contained V_{Mg}. In other words, these SCs were grown under Sn-rich condition. The calculation predicted that, as E_F approaches the top of the valence band, i.e., Mg_2Sn changes to p-type, the formation energy of Sn_{Mg} decreases and becomes even lower than that of V_{Mg} under the Sn-rich condition.[49] Initially, the Sn_{Mg} antisite defects are randomly distributed in the ingots. During the long cooling process, these antisite defects diffuse and aggregate without fracturing the crystal lattice. For this reason, the single-crystal region is partly transformed into the Sn-rich precipitate with the same crystal structure of the Mg_2Sn phase, similar to the formation of the V_{Mg} region. This mechanism will be examined by preparing Li-doped Mg_2Sn SCs using different growth conditions. The average size of the Sn-rich precipitates could be related to the Li-doping level. The GPA result of the R4 region in Figure 2a is shown in Figure 2h. Reflecting the endotaxial characteristic of the Sn-rich precipitates, no high-strain center was observed around the interface between the Sn-rich precipitate and the single-crystal region. From the above observations, we can conclude that there is no grain boundary in the prepared $Mg_{2-x}Li_xSn$ SCs in the nanoscopic level. The

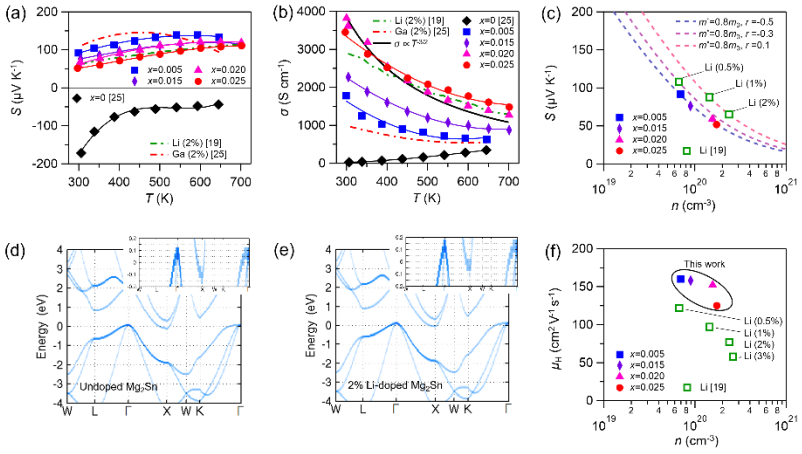

Figure 3. (a) Temperature dependence of the Seebeck coefficient *S* and (b) electrical conductivity σ of the $Mg_{2-x}Li_xSn$ (x = 0[25], 0.005, 0.015, 0.020, and 0.025) SCs, with the data of 2% Li-doped Mg_2Sn PC[19] and 2% Ga-doped Mg_2Sn SC.[25] (c) Pisarenko plot using *S* and carrier concentration *n* at 300 K. In (d) and (e), the electronic band structures of undoped Mg_2Sn and 2% Li-doped Mg_2Sn are shown. (f) Relation between carrier mobility, μ_H, and *n* at 300 K. For comparison, the data of Li-doped Mg_2Sn PCs[19] are plotted in (c) and (f).

interfaces between the V_{Mg} region/Sn-rich precipitates and the single-crystal region were semi-coherent or coherent.

Electronic transport properties

Figure 3a shows the temperature dependence of S of the $Mg_{2-x}Li_xSn$ (x = 0,[25] 0.005, 0.015, 0.020, and 0.025) SCs, together with that of the 2% Ga-doped Mg_2Sn SC[19] and the 2% Li-doped Mg_2Sn PC.[25] The x = 0 SC exhibited a negative S over the entire temperature range. In contrast, the sign of S at RT, S_{RT}, changed from negative to positive after doping with Li atoms, demonstrating that the Li-doping successfully prepared p-type Mg_2Sn SCs. Moreover, S_{RT} decreased from x = 0.005 to x = 0.025 SCs, indicating an increase in the hole carrier concentration. In fact, the carrier concentration n increased from 6.95×10^{19} cm^{-3} (x = 0.005) to 1.74×10^{20} cm^{-3} (x = 0.025) as shown in Table 1. The $Mg_{2-x}Li_xSn$ SCs with $x \geq 0.005$ presented a higher n than the 2% Ga-doped Mg_2Sn SC.[25] This result indicated that the E_F became much lower by the Li-doping relative to the Ga-doping, supporting that the Sn-rich precipitate was observed only in the $Mg_{2-x}Li_xSn$ SCs. Furthermore, carrier activation rate of the Li element in the Mg_2Sn SC was found to be higher than in the Ga element, as confirmed for the Li-doped Mg_2Sn PC.[19] However, the n of the $Mg_{2-x}Li_xSn$ SCs was lower than that of Li-doped Mg_2Sn PCs[19,20] when compared at similar Li content. Possible reasons for this difference in n are the presence of V_{Mg} and Sn-rich precipitate in the $Mg_{2-x}Li_xSn$ SCs. Considering that V_{Mg} induced hole carriers into Mg_2Sn SCs at a rate of 1×10^{17} cm^{-3} per percentage unit of the V_{Mg} fraction,[22] the lower n in the $Mg_{2-x}Li_xSn$ SCs relative to that of Li-doped Mg_2Sn PCs[19,20] is not due to V_{Mg} but to the Sn-rich precipitate. This is reasonable because the Sn_{Mg} is reported to induce electron carries into Mg_2Sn.[49,50] The above considerations indicate that V_{Mg} does not affect the electronic transport of hole carries in the $Mg_{2-x}Li_xSn$ SCs.

For the temperature dependence, the S first increased and then decreased with increasing temperature for the x = 0.005 and 0.015 SCs and the 2% Ga-doped Mg_2Sn SC[25] due to the bipolar effect. Furthermore, the temperature where the S reached a maximum value increased, indicating that the bipolar effect was suppressed according to the lowering of the E_F by the Li-doping. The suppression of the bipolar effect is beneficial to maintain the increasing tendency of S. Compared with the 2% Li-doped Mg_2Sn PC, the x = 0.020 SC exhibited higher S over the whole temperature range partly because of its lower n.

Figure 3b plots the temperature-dependent σ of the $Mg_{2-x}Li_xSn$ (x = 0,[25] 0.005, 0.015, 0.020, and 0.025) SCs. The data of the 2% Li-doped Mg_2Sn PC[19] and the 2% Ga-doped Mg_2Sn SC[25] are also presented for comparison. The temperature dependence of σ changed from an increasing tendency at x = 0[25] to a decreasing tendency for $x \geq 0.005$, suggesting that the Li-doping made the semiconducting Mg_2Sn SC degenerate semiconductors. With increasing the Li content x, σ increased mainly due to the increasing n (see Table 1). Compared with the 2% Li-doped Mg_2Sn PC,[25] the x = 0.020 SC showed higher σ from 300 K to 500 K and the x = 0.025 SC showed higher σ in the entire measurement temperature range. This is due to the higher μ_H of the $Mg_{2-x}Li_xSn$ SCs despite their lower n relative to the 2% Li-doped Mg_2Sn PC. Furthermore, all the $Mg_{2-x}Li_xSn$ SCs exhibited higher σ than the 2% Ga-doped Mg_2Sn SC,[25] attributed to the higher n and μ_H.

Table 1. Crystallinity/conduction type, carrier concentration n, carrier mobility μ_H, and existing secondary phase(s) of the prepared $Mg_{2-x}Li_xSn$ ingots and previously reported Mg_2Sn-based samples.[5,19,20,25,30] The abbreviations SC and PC stand for 'single crystal' and 'polycrystal', respectively.

	Crystallinity / conduction type	n (cm^{-3})	μ_H ($cm^2 \cdot V^{-1} \cdot s^{-1}$)	Secondary phase(s)
x = 0[25]	SC / n-type	1.68×10^{18}	93	Sn (edge area)
x = 0.005	SC / p-type	6.95×10^{19}	160	Sn (edge area)
x = 0.015	SC / p-type	8.94×10^{19}	158	Sn (edge area)
x = 0.020	SC / p-type	1.56×10^{20}	152	Sn (edge area)
x = 0.025	SC / p-type	1.74×10^{20}	124	Sn (edge area)
Ga (2%)[25]	SC / p-type	5.92×10^{19}	101	Sn
Ag (0.5%)[5]	Large-grain PC / p-type	5.9×10^{19}	~130	Mg+MgAg eutectic microstructures
Li (2%)[19]	PC / p-type	2.37×10^{20}	77	Not reported
Li (2.5%)[20]	PC / p-type	3.1×10^{20}	69	Sn, MgO
Na (2.5%)[20]	PC / p-type	1.1×10^{20}	82	Sn, MgO, t-Mg_9Sn_5+o-Mg_2Sn
Na (7%)[30]	PC / p-type	1.1×10^{20}	69	-

We investigated scattering mechanisms in their electronic transports to understand the difference in S and σ between the prepared SCs and reported PCs. The temperature dependence of σ of the x = 0.020 SC was well fitted by a relation $\sigma \propto T^{-3/2}$ (a bold black curve; Figure 3b), indicating that the dominant scattering mechanism for the x = 0.020 SC is acoustic phonon scattering (APS). On the other hand, the σ of the 2% Li-doped Mg_2Sn PC does not seem to obey such relation. In particular, the increasing trend of σ with decreasing temperature below 500 K is weakened compared to the x = 0.020 SC. A similar phenomenon is observed for several TE materials.[51–54] It is reported that the temperature dependence of σ is changed from an increasing trend into a decreasing one by reducing the grain size in a sample. This is because low energy carriers are scattered by a potential barrier at grain boundaries,[55,56] which is more pronounced at low temperatures. The so-called "energy filtering effect" causes the shallow increasing trend in σ of the 2% Li-doped Mg_2Sn PC, i.e., its electronic transport is governed by mixed scattering mechanisms of APS and grain boundary scattering (GBS).

We further examined the carrier scattering mechanisms using the Pisarenko plot, as shown in Figure 3c. The relation between S and n at 300 K of the $Mg_{2-x}Li_xSn$ (x = 0.005, 0.015, 0.020, and

0.025) SCs and Li-doped Mg_2Sn PCs[19] is plotted, together with calculated curves derived from an equation for a degenerate semiconductor expressed as:

$$S = \left[\frac{8\pi^{2/3}k_B^2(r+3/2)}{3^{5/3}eh^2}\right]\left(\frac{m^*}{n^{2/3}}\right)T, \quad \ldots(1)$$

where k_B, r, h, and m^* are the Boltzmann constant, scattering parameter (e.g., r = -1/2 for APS, 0 for neutral impurity scattering, 3/2 for ionized impurity scattering, …), Plank constant, and carrier effective mass, respectively. The data of the prepared SCs is on a curve with $m^* = 0.8m_0$ (m_0 is the free electron mass) and r = -1/2, verifying that APS is dominant in the prepared SCs. This result also indicates that the effective mass does not change much with the increase in the Li content, supported by calculation showing that valence band structures of undoped and 2% Li-doped Mg_2Sn are similar except for the E_F position (Figures 3d and 3e). Thus, we calculated S according to eq. (1), using $m^* = 0.8m_0$ and different r values (Figure 3c). As a result, the r values for the Li-doped Mg_2Sn PCs[19] are estimated to be between -0.3 and 0.1. These values are higher than r = -1/2, verifying that APS and GBS affect the electronic transport of the Li-doped Mg_2Sn PCs. It should be noted that the S value of the prepared SCs is lower than that of the Li-doped Mg_2Sn PCs[19] when compared at similar n values. From the above considerations, we can conclude that the lower S value is due to the absence of GBS and no energy filtering effect occurs in the prepared SCs.

Figure 3f shows the relation between carrier mobility, μ_H, and n at 300 K of the $Mg_{2-x}Li_xSn$ (x = 0.005, 0.015, 0.020, and 0.025) SCs and Li-doped Mg_2Sn PCs.[19] Due to the absence of GBS, the μ_H of the SCs in this work was higher than that of the PCs with comparable n. For example, the x = 0.005 SC and the 0.5% Li-doped Mg_2Sn PC had similar n, but the μ_H value for the former (160 $cm^2V^{-1}s^{-1}$) was 1.3 times higher than that for the latter (~ 120 $cm^2V^{-1}s^{-1}$). Here, we discuss the effect of the multi-scale defects on μ_H of the $Mg_{2-x}Li_xSn$ SCs. (1) The amount of Li is smaller than 2.5%, and hence the Li dopants have little effect on carrier scattering; (2) Although the V_{Mg} fraction in the $Mg_{2-x}Li_xSn$ SCs increased by the Li-doping (Figure 1c), V_{Mg} should not decrease μ_H because V_{Mg} is irrelevant to the electronic transport as mentioned before. In fact, in the case of undoped Mg_2Sn SCs, μ_H rather increased in spite of the increase of the V_{Mg} fraction.[22,34] The aggregation of V_{Mg}, i.e., the inhomogeneous distribution of V_{Mg} may help the transport of hole carriers in the single-crystal region without scattered by V_{Mg}; (3) Dislocations do not significantly reduce μ_H, because their density is as low as 3.3×10^{16} m^{-2}, which enables to form semi-coherent interface between the V_{Mg} region and the single-crystal region; (4) The Sn-rich precipitates do not scatter carriers, because the interface between the Sn-rich precipitate and the single-crystal region was coherent. Since the multi-scale defects did not deteriorate μ_H, the decrease of μ_H of the SCs and PCs with increasing the Li content can be ascribed to the increase of carrier-carrier scattering accompanied by the increase of hole carrier concentration. Thus, the high μ_H of the $Mg_{2-x}Li_xSn$ SCs is achieved by their high crystallinity without grain boundaries and ineffective nanostructures for electronic transport.

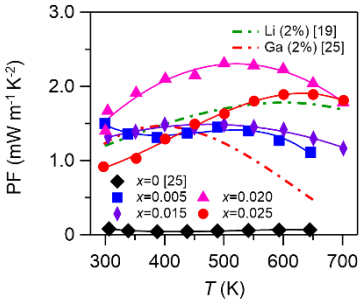

Figure 4. Power factor (PF) of the $Mg_{2-x}Li_xSn$ (x = 0[25], 0.005, 0.015, 0.020, and 0.025) SCs as a function of temperature. The data of 2% Li-doped Mg_2Sn PC[19] and 2% Ga-doped Mg_2Sn SC[25] are also shown.

The PF of the $Mg_{2-x}Li_xSn$ (x = 0,[25] 0.005, 0.015, 0.020, and 0.025) SCs are depicted as a function of temperature in Figure 4. Compared with the 2% Ga-doped Mg_2Sn SC[25], their PFs showed significant improvement except for the x = 0.025 SC at T < 450 K. The PF of the x = 0.020 SC was higher than that of the 2% Li-doped Mg_2Sn PC.[19] This increase can be attributed to higher S and σ. The x = 0.025 SC showed higher PF than the 2% Li-doped Mg_2Sn PC[19] above 550 K, reflecting the higher σ. Owing to the synergistic optimization of S and σ, we achieved maximum PF values of 2.2 $mW\cdot m^{-1}\cdot K^{-2}$ at 500 K for the x = 0.020 SC and 1.9 $mW\cdot m^{-1}\cdot K^{-2}$ at 650 K for the x = 0.025 SC.

Thermal transport properties

Figure 5a shows the temperature dependence of κ_{tot} of the $Mg_{2-x}Li_xSn$ (x = 0,[25] 0.005, 0.015, 0.020, and 0.025) SCs. At RT, κ_{tot} of all $Mg_{2-x}Li_xSn$ SCs was 6-6.5 $W\cdot m^{-1}\cdot K^{-1}$, which was lower than the 2% Li-doped Mg_2Sn PC[19] but higher than that of the 2% Ga-doped Mg_2Sn SC.[25] The x = 0.020 and 0.025 SCs exhibited lower κ_{tot} than the 2% Li-doped Mg_2Sn PC[19] over the entire temperature range. κ_{el} and κ_{bip} were calculated as a function of temperature using S, σ, and n (Figures S4 and S5, respectively). By subtracting κ_{el} and κ_{bip} from κ_{tot}, we obtained κ_{lat}, as shown in Figure 5b. The κ_{lat} decreased with x increased, and the x = 0.020 and 0.025 SCs showed a lower κ_{lat} than the 2% Ga-doped Mg_2Sn SC.[25] The lowest κ_{lat} was 1.2 $W\cdot m^{-1}\cdot K^{-1}$ at 650 K for the 0.025 SC.

To quantitatively understand the obtained low κ_{lat}, various phonon scattering processes were examined to calculate κ_{lat} for the x = 0.020 SC, based on the Debye Model.[57] We considered the Umklapp process (UP), and phonon scattering by point defects (PD), dislocation cores (DC), and nanoscale precipitate (NP). From the TEM observations described above, the strain fields were induced by the V_{Mg} in the x = 0.020 SC, and its effect was incorporated with the mass fluctuation to calculate a scattering parameter at the Mg site (Eq. (S18) in the Supporting Information). For the calculation of scattering parameters of DC and NP, the density of DCs and the average radius of NPs were used, respectively (Eqs. (S20) and (S21) in the Supporting Information). As shown in Figure 5c, the calculated κ_{lat} considering all phonon scatterings from UP, PD, DC, and NP agreed with the experimental κ_{lat}. The contribution of PD

scattering to the reduction of κ_{lat} was more significant than that of DC and NP scatterings. The contributions of PD, DC, and NP scattering at RT are 84%, 4%, and 12%. Thus, the additional NP scattering is the main reason for the lower κ_{lat} of the $Mg_{2-x}Li_xSn$ SCs compared to the 2% Ga-doped Mg_2Sn SC.[25]

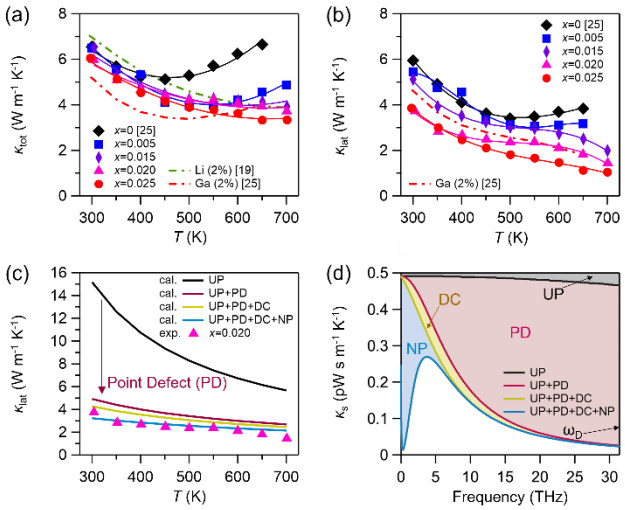

Figure 5. (a) Temperature dependence of the total thermal conductivity κ_{tot} and (b) lattice thermal conductivity κ_{lat} of the $Mg_{2-x}Li_xSn$ (x = 0[25], 0.005, 0.015, 0.020, and 0.025) SCs. The data of 2% Li-doped Mg_2Sn PC[19] and 2% Ga-doped Mg_2Sn SC[25] are also shown. (c) Comparison between the experimental and calculated κ_{lat} for the $Mg_{1.980}Li_{0.020}Sn$ (x = 0.020) SC. Phonon scattering from the Umklapp process (UP), point defects (PDs), dislocation cores (DCs), and nano precipitates (NPs) are considered in the calculation. (d) Frequency-dependent accumulative reduction in κ_{lat} (κ_s) of the $Mg_{1.980}Li_{0.020}Sn$ (x = 0.020) SC, considering the phonon scattering by UP, PDs, DCs, and NPs. ω_D is the Debye frequency.

To obtain further insight into the effect of each phonon scattering process on the κ_{lat} reductio, the frequency-dependent spectral lattice thermal conductivity (κ_s) was calculated according to:

$$\kappa_s(\omega) = \frac{k_B}{2\pi^2 v}\left(\frac{2\pi k_B T}{\hbar}\right)^3 \tau(\omega)\frac{x^4 e^x}{(e^x-1)^2}, x \equiv \frac{\hbar\omega}{k_B T}, \quad \ldots(2)$$

where v, $\hbar$, τ, and ω are the sound velocity, reduced Planck constant, relaxation time for phonon scattering, and phonon frequency, respectively. For the calculation, τ for UP or phonon scattering by PD, DC, or NP (eqs. (S14)-(S21) in the Supporting Information) was used. Figure 5d shows the κ_s curves of the x = 0.020 SC. The area between the two adjacent κ_s curves is equal to the reduction of κ_{lat} originating from the corresponding phonon scattering process. The κ_s of the UP showed a slight decrease with increasing ω. The PDs scattered the high-frequency phonons, as pointed out in the literature.[58] On the other hand, the DCs and NPs decreased κ_{lat} by scattering mid-frequency and low-frequency phonons, respectively. From these results, we can conclude that multi-scale defects in the $Mg_{2-x}Li_xSn$ SCs individually scattered phonons in a different frequency range. PDs, including V_{Mg}, played an important role in achieving the significant reduction of κ_{lat}.

Dimensionless figure-of-merit

Figure 6a shows the temperature dependence of zT of the $Mg_{2-x}Li_xSn$ (x = 0,[25] 0.005, 0.015, 0.020, and 0.025) SCs. The peak zT value increased with increasing the Li content x due to the optimization of the PF and κ_{tot}. Maximum zT values of 0.34 and 0.38 at 700 K were obtained for the x = 0.020 and x = 0.025 SCs, which were respectively 13% and 26% higher than that of p-type Mg_2Sn ever reported (the maximum zT ~ 0.3 [5,19]; Figure 6b). This study demonstrated that Mg_2Sn SCs with multi-scale defects are promising for n-type and p-type TE materials. The zT value of the $Mg_{2-x}Li_xSn$ SCs can be further enhanced by increasing the amount of V_{Mg} and subsequent dislocation cores, and the kind of nanoscale precipitates; for the former, additional B-doping should be an effective way, as reported for the B-doped Mg_2Sn and Mg_2Si SCs.[24]

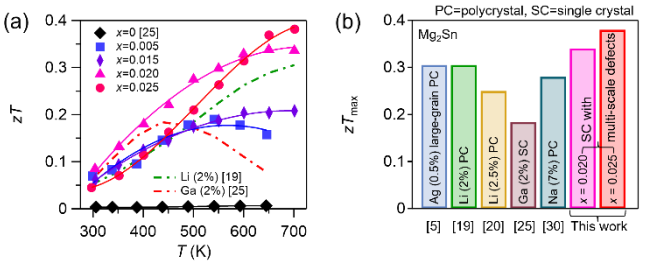

Figure 6. (a) Temperature dependence of the dimensionless figure-of-merit, zT, of the $Mg_{2-x}Li_xSn$ (x = 0[25], 0.005, 0.015, 0.020, and 0.025) SCs. The data of 2% Li-doped Mg_2Sn PC[19] and 2% Ga-doped Mg_2Sn SC[25] are also shown. (b) Comparison of maximum zT values zT_{max} of the x = 0.020 and 0.025 SCs with that of other p-type Mg_2Sn samples.

Conclusions

We prepared $Mg_{2-x}Li_xSn$ single crystals (SCs) and investigated the Li-doping effect on their crystal structure, nanostructure, and TE properties. All $Mg_{2-x}Li_xSn$ SCs contained V_{Mg} as a PD, and its fraction increased from 7.0(19)% to 14.0(30)% with the Li content x. In addition, dislocation cores and nanoscale Sn-rich precipitates existed in the $Mg_{2-x}Li_xSn$ SCs. These multi-scale defects did not deteriorate the electronic transport properties, i.e., S and σ. Rather, the $Mg_{2-x}Li_xSn$ SCs exhibited a high carrier mobility and a high PF benefiting from the absence of grain boundaries. The maximum PF for the x = 0.020 and 0.025 SCs were 2.2 $mW{\cdot}m^{-1}{\cdot}K^{-2}$ at 500 K and 1.9 $mW{\cdot}m^{-1}{\cdot}K^{-2}$ at 650 K, respectively. On the other hand, the κ_{lat} was significantly affected by the multi-scale defects. PDs, DCs, and NPs scattered the phonons with different frequencies making the κ_{lat} of the $Mg_{2-x}Li_xSn$ SCs lower than the undoped and elementary-doped Mg_2Sn PCs and SCs. Consequently, the highest zT value among the p-type Mg_2Sn was achieved for the x = 0.025 SC (zT = 0.38 at 700 K). This study demonstrates that multi-scale defects engineering enhanced the TE performance of p-type Mg_2Sn.

Author Contributions

Zhicheng Huang: Conceptualization, methodology, data curation, formal analysis, investigation, writing-original draft,

writing-review & editing, funding acquisition. Kei Hayashi: Supervision, project administration, data curation, investigation, writing-review & editing, funding acquisition. Wataru Saito: Data curation, formal analysis, funding acquisition. Jun Pei: Formal analysis. Jing-Feng Li: Project administration, validation, writing-review & editing. Yuzuru Miyazaki: Supervision, project administration, writing-review & editing.

Conflicts of interest

There are no conflicts to declare.

Acknowledgements

This work was partly supported by the Grant-in-Aid for JSPS Fellows from the Japan Society for the Promotion of Science (No. 20J10512), JST SPRING from the Japan Science and Technology Agency (No. JPMJSP2114), and Grant-in-Aid for Scientific Research (B) from the Ministry of Education, Culture, Sports, Science, and Technology of Japan (Nos. 17H03398, 22H02161). This work was partly based on collaborative research between Sumitomo Metal Mining Co., Ltd. and Tohoku University, which is part of the Vision Co-creation Partnership.

Notes and references

1 D. M. Rowe, *Thermoelectrics handbook: macro to nano*, CRC press, 2018.
2 Z. Ren, Y. Lan and Q. Zhang, *Advanced thermoelectrics: materials, contacts, devices, and systems*, CRC Press, 2017.
3 K. Hayashi, Y. Miyazaki, W. Saito, M. Kubouchi, Y. Ogawa, S. Suzuki, Y. Hayashibara and I. Ando, *Thermoelectr. Mater.*, 2020, 99–116.
4 K. Hayashi, H. Li, M. Eguchi, Y. Nagashima, Y. Miyazaki and D. R. Sahu, Magnetic *Magn. Mater. Magn. Levitation*, 2020, 65.
5 H. Y. Chen, N. Savvides, T. Dasgupta, C. Stiewe and E. Mueller, *Phys. Status Solidi Appl. Mater. Sci.*, 2010, **207**, 2523–2531.
6 H. Ihou-Mouko, C. Mercier, J. Tobola, G. Pont and H. Scherrer, *J. Alloys Compd.*, 2011, **509**, 6503–6508.
7 T. H. An, S. M. Choi, I. H. Kim, S. U. Kim, W. S. Seo, J. Y. Kim and C. Park, *Renew. Energy*, 2012, **42**, 23–27.
8 W. Liu, K. Yin, X. Su, H. Li, Y. Yan, X. Tang and C. Uher, *Intermetallics*, 2013, **32**, 352–361.
9 M. B. A. Bashir, S. Mohd Said, M. F. M. Sabri, D. A. Shnawah and M. H. Elsheikh, *Renew. Sustain. Energy Rev.*, 2014, **37**, 569–584.
10 S. Kim, B. Wiendlocha, H. Jin, J. Tobola and J. P. Heremans, *J. Appl. Phys.*, 2014, **116**, 0–8.
11 H. Ning, G. D. Mastrorillo, S. Grasso, B. Du, T. Mori, C. Hu, Y. Xu, K. Simpson, G. Maizza and M. J. Reece, *J. Mater. Chem. A*, 2015, **3**, 17426–17432.
12 P. Gao, J. D. Davis, V. V. Poltavets and T. P. Hogan, *J. Mater. Chem. C*, 2016, **4**, 929–934.
13 Y. R. Jin, Z. Z. Feng, L. Y. Ye, Y. L. Yan and Y. X. Wang, *RSC Adv.*, 2016, **6**, 48728–48736.
14 M. Kubouchi, K. Hayashi and Y. Miyazaki, *Scr. Mater.*, 2016, **123**, 59–63.
15 W. Liu, J. Zhou, Q. Jie, Y. Li, H. Seok Kim, J. Bao, G. Chen and Z. Ren, *Energy Environ. Sci.*, 2016, **9**, 530–539.
16 J. de Boor, T. Dasgupta, U. Saparamadu, E. Müller and Z. F. Ren, *Mater. Today Energy*, 2017, **4**, 105–121.
17 U. Saparamadu, J. de Boor, J. Mao, S. Song, F. Tian, W. Liu, Q. Zhang and Z. Ren, *Acta Mater.*, 2017, **141**, 154–162.
18 Y. Hayashibara, K. Hayashi, I. Ando, M. Kubouchi, Y. Ogawa, W. Saito and Y. Miyazaki, *Materials, Mater. Trans.*, 2018, **59**, 1041-1045.
19 H. Kamila, P. Sahu, A. Sankhla, M. Yasseri, H. N. Pham, T. Dasgupta, E. Mueller and J. De Boor, *J. Mater. Chem. A*, 2019, **7**, 1045–1054.
20 J. ichi Tani, T. Shinagawa and M. Chigane, *J. Electron. Mater.*, 2019, **48**, 3330–3335.
21 K. Hayashi, W. Saito, K. Sugimoto, K. Ohoyama, K. Hayashi, N. Happo, M. Harada, K. Oikawa, Y. Inamura and Y. Miyazaki, *AIP Adv.*, 2020, **10**, 035115.
22 W. Saito, K. Hayashi, J. Dong, J.-F. Li & Y. Miyazaki, *Sci. Rep.*, 2020, **10**, 2020.
23 W. Saito, K. Hayashi, Z. Huang, J. Dong, J. F. Li and Y. Miyazaki, *ACS Appl. Mater. Interfaces*, 2020, **12**, 57888–57897.
24 W. Saito, K. Hayashi, Z. Huang, K. Sugimoto, K. Ohoyama, N. Happo, M. Harada, K. Oikawa, Y. Inamura, K. Hayashi, T. Miyazaki and Y. Miyazaki, *ACS Appl. Energy Mater.*, 2021, **4**, 5123–5131.
25 Z. Huang, K. Hayashi, W. Saito and Y. Miyazaki, *ACS Appl. Energy Mater.*, 2021, **4**, 13044–13050.
26 Y. Zhu, E. Dong, Z. Han, F. Jiang, J. Sui, W. Zhang and W. Liu, *Acta Mater.*, 2021, **217**, 117172.
27 Y. Zhu, Z. Han, F. Jiang, E. Dong, B. P. Zhang, W. Zhang and W. Liu, *Mater. Today Phys.*, 2021, **16**, 100327.
28 Y. Zhu, Z. Han, B. Han, F. Jiang, X. Wu, C. G. Han, Y. Deng and W. Liu, *ACS Appl. Mater. Interfaces*, 2021, **13**, 56164–56170.
29 M. Safavi, N. Martin, E. Aubry, V. Linseis, A. Billard and M. Arab Pour Yazdi, *J. Electron. Mater.*, 2021, **50**, 2738–2749.
30 Y. Huang, S. Zheng, H. Liao, S. Qiao, G. Han, G. Wang, Z. Huang, J. Li, X. Lu and X. Zhou, *J. Mater. Chem. A*, 2022, **10**, 5452–5459.
31 K. Cheng, Z. Bu, J. Tang, X. Zhang, X. Meng, W. Li and Y. Pei, *Mater. Today Phys.*, 2022, **28**, 100887.
32 J. Mao, Y. Wang, B. Ge, Q. Jie, Z. Liu, U. Saparamadu, W. Liu and Z. Ren, *Phys. Chem. Chem. Phys.*, 2016, **18**, 20726–20737.
33 J. Xin, Y. Zhang, H. Wu, T. Zhu, T. Fu, J. Shen, S. J. Pennycook and X. Zhao, *Small Methods*, 2019, **3**, 1900412.
34 K. Hayashi, *JSAP Rev.*, 2022, **2022**, 220403.
35 W. He, T. Hong, D. Wang, X. Gao and L.-D. Zhao, *Sci. China Mater.*, 2021, **64**, 3051–3058.
36 K. Imasato, C. Fu, Y. Pan, M. Wood, J. J. Kuo, C. Felser and G. J. Snyder, *Adv. Mater.*, 2020, **32**, 1908218.
37 C. Tang, Z. Huang, J. Pei, B. P. Zhang, P. P. Shang, Z. Shan, Z. Zhang, H. Gu and K. Wen, *RSC Adv.*, 2019, **9**, 14422–14431.
38 Y. Wu, J. Pei, R. Zhang, Z.-C. Huang, Z. Zhao and B.-P. Zhang, *J. Alloys Compd.*, 2020, **830**, 154451.
39 M. Kubouchi, K. Hayashi and Y. Miyazaki, *J. Alloys Compd.*, 2014, **617**, 389–392.
40 M. Kubouchi, Y. Ogawa, K. Hayashi, T. Takamatsu and Y. Miyazaki, *J. Electron. Mater.*, 2016, **45**, 1589–1593.
41 V. Petříček, M. Dušek and L. Palatinus, *Z. Für Krist. - Cryst. Mater.*, 2014, **229**, 345–352.
42 AkaiKKR machikaneyama, Ab-initio electronic-structure calculation code. http://kkr.issp.u-tokyo.ac.jp/ (accessed 2/16, 2022).
43 T. Inoue, S. Chikazumi, S. Nagasaki and S. Tanuma, *AGNE Technol. Cent. Tokyo Jpn.*, 2001.

44 W. D. Callister, D. G. Rethwisch, and others, *Materials science and engineering: an introduction*, Wiley New York, 2018, vol. 9.
45 I.-L. Jen, K.-K. Wang and H.-J. Wu, *Adv. Sci.*, 2022, **9**, 2201802.
46 H. Wu, F. Zheng, D. Wu, Z. H. Ge, X. Liu and J. He, *Nano Energy*, 2015, **13**, 626–650.
47 M. J. Hÿtch, E. Snoeck and R. Kilaas, *Ultramicroscopy*, 1998, **74**, 131–146.
48 G. A. Jones and L. D. Keigwin, *Nature*, 1988, **336**, 56–59.
49 X. Liu, L. Xi, W. Qiu, J. Yang, T. Zhu, X. Zhao and W. Zhang, *Adv. Electron. Mater.*, 2016, **2**, 1500284.
50 B. Ryu, E.-A. Choi, S. Park, J. Chung, J. de Boor, P. Ziolkowski, E. Müller and S. Park, *J. Alloys Compd.*, 2021, **853**, 157145.
51 J. de Boor, T. Dasgupta, H. Kolb, C. Compere, K. Kelm and E. Mueller, *Acta Mater.*, 2014, **77**, 68–75.
52 J. Shuai, J. Mao, S. Song, Q. Zhu, J. Sun, Y. Wang, R. He, J. Zhou, G. Chen, D. J. Singh and Z. Ren, *Energy Environ. Sci.*, 2017, **10**, 799–807.
53 Y. Wu, F. Liu, Q. Zhang, T. Zhu, K. Xia and X. Zhao, *J. Mater. Chem.*, 2020, **8**, 8455–8461.
54 C. Hu, K. Xia, C. Fu, X. Zhao and T. Zhu, *Energy Environ. Sci.*, 2022, **15**, 1406–1422.
55 J. Y. W. Seto, *J. Appl. Phys.*, 1975, **46**, 5247–5254.
56 J. P. Heremans, C. M. Thrush and D. T. Morelli, *Phys. Rev. B*, 2004, **70**, 115334.
57 J. Callaway and H. C. von Baeyer, *Phys. Rev.*, 1960, **120**, 1149–1154.
58 Z. Chen, X. Zhang and Y. Pei, *Adv. Mater.*, 2018, **30**, 1705617.